

High-resolution grazing-incidence x-ray diffraction for characterization of defects in crystal surface layers

E. A. Kondrashkina,^{a),b)} S. A. Stepanov,^{a)} M. Schmidbauer, R. Opitz, and R. Köhler
MPG-AG "Röntgenbeugung," Hausvogteiplatz 5-7, Berlin D-10117, Germany

H. Rhan

HASYLAB/DESY, Notkestrasse, 85, Hamburg D-22549, Germany

(Received 24 June 1996; accepted for publication 24 September 1996)

The peculiarities of high-resolution measurements in grazing-incidence diffraction (GID) are studied, both theoretically and experimentally. It is shown that complete discrimination between coherent reflection and diffuse scattering due to defects in GID requires a three-dimensional mapping of reciprocal space. These measurements can be performed using a combination of analyzer crystal and position-sensitive detector for angular analysis of scattered x-rays in mutually perpendicular planes. The equations for the resolution function of GID experiments are given and applied to the interpretation of GID measurements taken from an AlAs/GaAs superlattice. The discrimination of diffuse scattering due to interfacial roughness in the superlattice is demonstrated.

© 1997 American Institute of Physics. [S0021-8979(97)02801-6]

I. INTRODUCTION

It is commonly nowadays recognized that grazing-incidence x-ray diffraction (GID)¹⁻⁴ is superior to conventional x-ray diffraction techniques in the study of the crystal structure of thin surface layers. GID has been successfully applied to studies of surface treatment,⁵ oxidation⁶ and ion implantation⁷⁻¹⁰ of semiconductor wafers and to the analysis of strain relaxation in epitaxial layers^{1,11,12} and multilayers.^{13,14} The high brightness of third generation x-ray synchrotron sources provides an opportunity to perform high-resolution measurements in GID by analogy with high-resolution diffractometry and reciprocal space mapping in the conventional Bragg case.¹⁵⁻²⁷ This suggests a new qualitative level of data on structure and defects in thin surface layers accessible with GID.

Up to now, the experimental techniques of GID measurements have been mainly confined to two double-crystal schemes. In both of them the incident beam is collimated in the incidence angle in order to provide penetration depth of the x-rays into the sample as required. The difference is that in one scheme [Fig. 1(a)] the incident beam is not collimated in the Bragg plane and the diffracted waves are analyzed depending on their takeoff angle to the surface,^{2,5,10,28-31} while in the other one [Fig. 1(b)] the incident beam is collimated in the Bragg plane and the dependence of diffracted beam intensity on deviation of the sample from the Bragg position^{1,3,4,11,12} is studied. In both cases, diffracted intensity is registered integrally with diffuse scattering caused by structural defects and interface roughness. As a result, the interpretation of diffraction data on crystal lattice strains is impeded and information on structural defects contained in the diffuse scattering is lost.

In conventional high-resolution diffractometry, the separation of coherent and diffuse scattering is implemented with

the help of an analyzer crystal.^{15,16} The sample is set at different deviations from the Bragg condition for the incident x-ray beam and the analyzer scans the angular spectrum of diffracted x-rays in the plane of diffraction.¹⁵⁻²⁷ Such scans provide a two-dimensional (2D) mapping of reciprocal space in the plane of diffraction. The information is integrated along the direction perpendicular to this plane, but it is not very important because there are no physical reasons for considerable out-of-plane changes in x-ray scattering in the conventional geometries of diffraction. However, it has recently been suggested that in conventional Bragg diffraction three-dimensional (3D) mapping of reciprocal space could provide additional information on defects in crystals.^{32,33}

In grazing-incidence diffraction, the problem of discriminating between coherent and diffuse x-ray scattering is qualitatively different because the plane of diffraction runs parallel or nearly parallel to the crystal surface and the intensity of x-ray scattering strongly depends on deviations of the scattered waves from this plane (Fig. 1). For example, x-rays leaving the crystal at different takeoff angles with respect to the surface carry structural information from different depths of the sample. Thus, in GID an analysis of scattered radiation over the takeoff angle [Fig. 1(c)] may turn out to be more informative than that in the plane of diffraction [Fig. 1(d)]. However, maximum information on structure and defects of surface layers can be obtained in GID only with the 2D angular analysis of scattered x-rays at different deviations of incident x-rays from the Bragg condition [Fig. 1(e)]. The last scheme corresponds to a 3D mapping of reciprocal space.³⁴

The peculiarities of high-resolution measurements in GID schemes shown in Fig. 1(c) and 1(d) were studied by Afanas'ev *et al.*³⁵⁻³⁷ The theory and the experiments, however, were restricted to the range of so-called Bragg-Laue grazing-incidence diffraction, where incident and diffracted beams as well as the reciprocal lattice vector make angles of several degrees with respect to the surface and specular reflection effects are negligible. The positions of the coherent

^{a)}Permanent address: Institute for Nuclear Problems, 11 Bobruiskaya St., Minsk 220050, Republic of Belarus.

^{b)}Electronic mail: elena@x-ray0.roen.ipp-garching.mpg.de

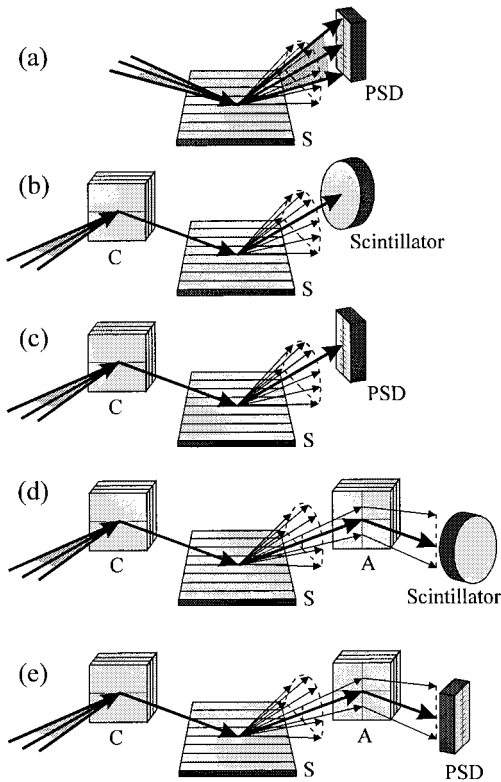


FIG. 1. Different experimental schemes of grazing-incidence x-ray diffraction: (a), (b) no separation of coherent and diffuse scattering; (c), (d) partial separation; (e) complete separation. Coherent waves are shown by thick arrows and diffuse scattering by thin arrows. The collimator, sample and analyzer crystals are denoted by the letters C, S and A respectively. PSD is the position sensitive detector.

peaks on the high-resolution Bragg-Laue diffraction curves were calculated and measured for perfect and boron implanted Si crystals. It was found that in the case of a laterally nondeformed crystal, the measurements in schemes (c) and (d) of Fig. 1 are equivalent in the discrimination of coherent diffraction. However, as shown in Section II of this article, this equivalency does not hold when the lateral lattice spacing in the sample is not constant over the sample volume (relaxed multilayers, etc.). Besides, as explained above, schemes (c) and (d) in Fig. 1 cannot be equivalent in the mapping of diffuse scattering because they provide maps in essentially different planes.

A GID study of lattice relaxation in GaInAs/GaAs superlattices was carried out in Refs. 13 and 14 with the application of the experimental scheme corresponding to Fig. 1(c). However, the experimental setup was not optimized: the use of different Bragg reflections for the collimator and sample resulted in a strong dispersion effect and a drastic deterioration of the resolution function. This reduced the measurements to the low-resolution case (a) rather than the high-resolution case (c) in Fig. 1.

An analysis of Huang diffuse scattering in GID from defects in ion-implanted Si crystals was undertaken in Refs. 9 and 38 on the basis of an experimental scheme similar to (d) and (e) in Fig. 1. As was evident from the curves presented, the resolution of the experiments was rather poor. The schemes were dispersive and the collimation of the in-

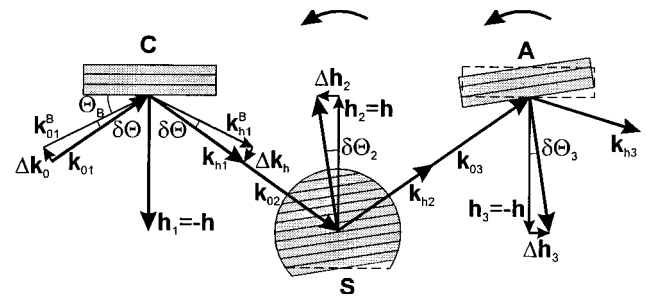


FIG. 2. The derivation of coherent peaks positions in high-resolution GID experiment. The collimator, sample and analyzer crystals are denoted by the letters C, S and A and the vectors related to them are marked as 1, 2 and 3 respectively. The reciprocal lattice vectors \mathbf{h}_1 , \mathbf{h}_2 , \mathbf{h}_3 and wave vectors \mathbf{k}_{01} , $\mathbf{k}_{h1}=\mathbf{k}_{02}$ lie in the plane of the figure, while wave vectors $\mathbf{k}_{h2}=\mathbf{k}_{03}$, \mathbf{k}_{h3} and the sample surface are slightly deflected from this plane.

cident beam in the diffraction plane was determined by slits behind the monochromator. The analyzer crystal in Fig. 1(e) was also replaced with slits. Therefore, essential details of the scattering were not accessible.

As evidenced above, there is a need for a methodological study on the resolution function (the position and the width of coherent peaks) of high-resolution measurements in different experimental schemes of GID. In Section II a theoretical analysis is given on the formation of high-resolution GID patterns in the schemes corresponding to (c) and (e) in Fig. 1. In Section III the high-resolution measurements in schemes (c) and (e) of GID are described. The measurements were carried out for a perfect Ge crystal and a GaAs/AlAs superlattice. In Section IV the experimental data are compared to theory and possible ways to optimize the resolution function for the discrimination of diffuse scattering in GID are discussed.

II. THEORY

In order to describe the formation of high-resolution GID patterns, one has to find deviations of the x-rays from their exact Bragg conditions when they are successively diffracted by three crystals (Fig. 2). Let us assume that the crystals in Fig. 2 are initially aligned in such a way that the reciprocal vectors \mathbf{h}_1 , \mathbf{h}_2 and \mathbf{h}_3 are parallel to each other and lie in the plane of the figure. The incident wave vector \mathbf{k}_{01} is also aligned in this plane. We assume that there is a symmetrical Bragg-case diffraction at crystals 1 and 3 and GID at crystal 2. Then, the surfaces of crystals 1 and 3 are perpendicular to the plane of Fig. 2, while the surface of crystal 2 is nearly parallel to it. The latter makes a small angle Φ_0 with the wave vector $\mathbf{k}_{h1}=\mathbf{k}_{02}$, which belongs to the plane of the figure. Due to the non-coplanar grazing-incidence reflection from crystal 2, vectors $\mathbf{k}_{h2}=\mathbf{k}_{03}$ and \mathbf{k}_{h3} generally deviate by a small angle from the plane of the figure.

Now, let us assume that the incident vector \mathbf{k}_{01} is turned away from the exact Bragg position by a small angle $\delta\theta$ and vectors \mathbf{h}_2 and \mathbf{h}_3 are turned away from their initial parallel position by the small angles $\delta\theta_2$ and $\delta\theta_3$ respectively, as shown in Fig. 2. Then, one can find

$$\alpha_1 = \frac{(\mathbf{k}_{01}^B + \Delta\mathbf{k}_0 + \mathbf{h}_1)^2 - k_0^2}{k_0^2} \approx -\frac{2(\Delta\mathbf{k}_0 \cdot \mathbf{h}_1)}{k_0^2} \approx -2 \sin(2\theta_B) \delta\theta, \quad (1)$$

$$\alpha_2 = \frac{(\mathbf{k}_{h1} + \mathbf{h}_2 + \Delta\mathbf{h}_2)^2 - k_0^2}{k_0^2} \approx -2 \sin(2\theta_B) (\delta\theta + \delta\theta_2), \quad (2)$$

$$\alpha_3 = \frac{(\mathbf{k}_{h2} + \mathbf{h}_3 + \Delta\mathbf{h}_3)^2 - k_0^2}{k_0^2} = \frac{(\mathbf{k}_{h2\parallel} + \mathbf{h}_{3\parallel} + \Delta\mathbf{h}_3)^2 + (k_{h2z} + h_{3z})^2 - k_0^2}{k_0^2} \approx (\Phi_h + \psi_2)^2 - \Phi_0^2 - 2 \sin(2\theta_B) (\delta\theta_2 - \delta\theta_3). \quad (3)$$

Here α_i are the standard parameters of the deviations of x-rays from the Bragg condition at the three crystals, Φ_h is the takeoff angle of \mathbf{k}_{h2} with respect to the sample surface, $\psi_2 = h_{2z}/k_0 = 2\varphi_2 \sin\theta_B$ and φ_2 is the miscut angle of the sample. The vectors in (3) are expanded over the components normal (z) and parallel (\parallel) to the surface of crystal 2.

Now, let us consider a sample with a constant lateral lattice spacing or a multilayer consisting of a stack of crystalline layers with laterally matched lattice spacing (the lattice spacing along the surface normal can vary arbitrarily). Then, the following relation holds:^{2,39,40,41}

$$\Phi_h^2 = (\Phi_0 + \psi_2)^2 - \alpha_2. \quad (4)$$

Substituting (4) into (1)–(3) and proceeding from $\delta\theta$ to the angle $\delta\theta' = \delta\theta + \delta\theta_2$, which determines the deviation of the incident x-ray beam from the Bragg condition for the sample, we find

$$\alpha_1 = (\Phi_0 + \psi_2)^2 - \Phi_h^2 - \alpha(\delta\theta_2), \quad (5)$$

$$\alpha_2 = (\Phi_0 + \psi_2)^2 - \Phi_h^2, \quad (6)$$

$$\alpha_3 = (\Phi_h + \psi_2)^2 - \Phi_0^2 - \alpha(\delta\theta'_3), \quad (7)$$

where $\delta\theta'_3 = \delta\theta_3 - \delta\theta_2$ is the angular offset between the analyzer and the sample, and $\alpha(\delta\theta) = -2 \sin(2\theta_B)\delta\theta$.

Eqs. (4) and (5)–(7) can be used for the analysis of grazing-incidence diffraction curves in the schemes shown in Figs. 1(a), 1(c), and 1(e).

In Fig. 1(a) the beam incident onto the sample is uniformly spread over $\delta\theta$. Therefore, the diffracted x-rays taking off from the sample at $\Phi_h(\delta\theta)$ are characterized by a relative intensity proportional to the respective reflection coefficient $P_{\text{GID}}(\delta\theta)$, and the reflection curve of the sample can be recorded as a function of the angle Φ_h . As follows from (4), the variations of the takeoff angle $\delta\Phi_h = \sin(2\theta_B)\delta\theta/\Phi_h \approx (10^2 - 10^3)\delta\theta$ are several orders of magnitude greater than that of the in-plane angle $\delta\theta$. Therefore, no analyzer crystal is necessary and one can record GID curves over the takeoff angle using a slit in front of the scintillation detector or the position sensitive detector (PSD). The data set taken by PSD will be

$$P_1^{\text{PSD}}(\Phi_h) \approx P_{\text{GID}}(\alpha_2). \quad (8)$$

This way of recording GID curves was first proposed in Ref. 2 and used in Refs. 5, 10, and 28–31.

In the case of Fig. 1(c), the angular distribution of the beam arriving at the sample is no longer uniform and the PSD records a product of two reflection coefficients:

$$P_2^{\text{PSD}}(\Phi_h) \approx P(\alpha_1)P_{\text{GID}}(\alpha_2), \quad (9)$$

where $P(\alpha_1)$ is the Bragg-reflection rocking curve of the collimator crystal (the Darwin curve).

Finally, in the case of Fig. 1(e) the PSD spectrum is determined by a product of the three reflection coefficients:

$$P_3^{\text{PSD}}(\Phi_h) \approx P(\alpha_1)P_{\text{GID}}(\alpha_2)P(\alpha_3). \quad (10)$$

As follows from (5)–(7), the PSD spectrum in the case of Fig. 1(e) can consist of a collimator, a sample and analyzer peaks. The positions of the collimator and analyzer peaks given by $\alpha_1=0$ and $\alpha_3=0$ respectively, read

$$\Phi_h^{\text{clm}} = \sqrt{(\Phi_0 + \psi_2)^2 - \alpha(\delta\theta_2)}, \quad (11)$$

$$\Phi_h^{\text{anl}} = -\psi_2 \pm \sqrt{\Phi_0^2 + \alpha(\delta\theta'_3)}. \quad (12)$$

Eqs.(11) and (12) show that the collimator and analyzer peaks may be missing in the spectra at great $\delta\theta_2 < 0$ and $\delta\theta'_3 > 0$ respectively. On the other hand, at $\psi_2 < 0$ (when the reciprocal vector of GID points towards outside the sample) there might be two analyzer peaks.

The sample peak is near $\alpha_2=0$, i.e. $\Phi_h^B = |\Phi_0 + \psi_2|$, but at $\Phi_0 \approx \Phi_c$ or $\Phi_h^B \approx \Phi_c$, where Φ_c is the critical angle of specular reflection, the position of the peak can be shifted from Φ_h^B due to refraction effects. The shift can be up to $\pm\Phi_c$ and in most cases the sample peak appears near Φ_c , if $\Phi_h^B \lesssim \Phi_c$. For example, at $\psi_2=0$ and $\Phi_0 \lesssim \Phi_c$ the peak position $(0.7-0.8)\Phi_c$ is given by the total reflection threshold for one of the roots of the dispersion equation of GID.² In general, the sample rocking curve $P_{\text{GID}}(\delta\theta)$ and the position of the sample peak can be calculated numerically with the matrix method.^{31,39-42} For a periodic multilayer, there are many sample peaks at Φ_h coinciding with different-order Bragg angles for the multilayer.

Eqs. (1)–(3) allow one to calculate the positions of the collimator peak and the sample peak at three-crystal spectra in the case of Fig. 1(d). For the sample peak, the condition $\alpha_2=\alpha_3=0$ yields $\delta\theta_3=\delta\theta_2$, and the position of the collimator peak given by $\alpha_1=\alpha_3=0$ is

$$\delta\theta_3 = -\frac{\psi_2(\Phi_0 + \Phi_h + \psi_2)}{\sin(2\theta_B)}, \quad (13)$$

where $\Phi_h = [(\Phi_0 + \psi_2)^2 - \alpha(\delta\theta_2)]^{1/2}$. In Bragg-Laue geometry ($\psi_2 < 0$, $|\psi_2| > \Phi_0$, $|\psi_2| > \Phi_h$) formula (13) is reduced to $\delta\theta'_3 = |\psi_2|(\Phi_h - \Phi_h^B)/\sin(2\theta_B)$ found in Ref. 35.

In the case of lateral lattice spacing variations in the sample the structure of high-resolution GID pattern becomes more complicated.⁴³ Consider, e.g., a sample with a relaxed epilayer. The relaxation usually results in a difference of lattice parameters $\Delta a/a \sim 10^{-3} - 10^{-1}$. That corresponds to a difference in the Bragg angles exceeding by far the width of the Bragg peaks. Hence, the diffraction from the substrate

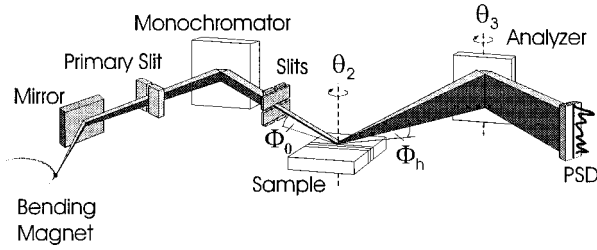


FIG. 3. Schematic drawing of a high-resolution GID experiment carried out on the D4 beamline at HASYLAB. In the first stage of measurements the analyzer crystal was removed and PSD spectra were measured over the takeoff angle Φ_h at different deviations $\delta\theta_2$ of the sample from the Bragg angle. In the second stage of the experiment the PSD spectra were taken at different $\delta\theta_2$ and different deviations $\delta\theta_3$ of the analyzer.

and the layer can be treated independently and, in addition to (5)–(7) for the substrate, we have the following relations for the mismatched layer:

$$\alpha_1 = (\Phi_0 + \psi_2)^2 - \Phi_h^2 - \alpha(\delta\theta_2) - \alpha(\Delta a/a), \quad (14)$$

$$\alpha_2 = (\Phi_0 + \psi_2)^2 - \Phi_h^2, \quad (15)$$

$$\alpha_3 = (\Phi_h + \psi_2)^2 - \Phi_0^2 - \alpha(\delta\theta'_3) - \alpha(\Delta a/a). \quad (16)$$

Here is $\alpha(\Delta a/a) = -4 \sin^2(\theta_B)\Delta a/a$. We see that in the case of lattice mismatch, the peak from the layer remains at the same position in the PSD spectra as that from the substrate [see Eqs. (6) and (15)]. Thus, measurements of $\Delta a/a$ are not possible in the scheme of Fig. 1(a). However, both the collimator and the analyzer peaks split due to the lattice mismatch and new peaks are shifted by $\approx \sqrt{\alpha(\Delta a/a)}$ from their original positions. At $\Delta a/a \approx 10^{-4}$ the shift is $\approx 10^{-2}$. Thus, one can measure the crystal lattice relaxation with high precision by analyzing the PSD spectra in schemes (c) and (e) in Fig. 1.

In some experiments vector \mathbf{h}_3 might be misaligned from the plane of Fig. 2 because the precise alignment of the analyzer crystal is impeded by the double-plane collimation of the incident x-ray beam and the non-coplanar reflection from the sample. In the case of misalignment of the analyzer by an angle φ_3 , Eqs. (3) and (12) are generalized as

$$\alpha_3^{\text{mis}} = (\Phi_h - \psi_3)^2 - \Phi_0^2 - \alpha(\delta\theta'_3) - (\psi_3^2 - \psi_2^2)/2, \quad (17)$$

$$\Phi_h^{\text{anl}} = \psi_3 \pm \sqrt{\Phi_0^2 + \alpha(\delta\theta'_3) + (\psi_3^2 - \psi_2^2)/2}, \quad (18)$$

where $\psi_3 = h_{3z}/k_0 = 2(\varphi_3 - \varphi_2)\sin\theta_B$.

III. EXPERIMENT

High-resolution measurements of GID have been performed at the D4 beamline of HASYLAB, DESY. The experimental setup is shown in Fig. 3. The measurements were carried out with and without an analyzer crystal (the schemes corresponded to Fig. 1(e) and 1(c), respectively). The monochromator, sample and analyzer were set in a non-dispersive parallel (n,n,n) arrangement and the GID curves were recorded by a PSD.

A single-bounce Ge monochromator adjusted for (220) Bragg reflection selected synchrotron radiation with a wavelength of 1.55 Å (the higher harmonics of radiation were

suppressed by a mirror installed at the entrance of the beamline). Due to the absence of dispersion, the horizontal divergence of the beam incident onto the sample after reflection from the monochromator was defined by the width of the monochromator Darwin curve, which corresponded to 0.002°. The front of the beam in the horizontal direction was formed by the vertical 1 mm slit placed behind the monochromator. The beam divergence in vertical plane was about 0.004°, as defined by the initial vertical size of the synchrotron beam of 1.3 mm and the horizontal slit of 0.05 mm located behind the monochromator at a distance of about 21 m from the bending magnet. Thus, the beam incident onto the sample was collimated in both the vertical and the horizontal planes, i.e. in the plane of beam incidence and in the diffraction plane.

Two different samples were chosen: a perfect Ge(001) crystal and an AlAs/GaAs(001) superlattice. The surfaces of both samples had a small miscut φ_2 of about 0.30° and 0.38° respectively. The superlattice consisted of 20 periods of 154 Å AlAs and 73 Å GaAs grown on a GaAs substrate by means of molecular beam epitaxy. The superlattice had been studied by x-ray reflectivity techniques in the laboratory and diffuse scattering from interfacial roughness was revealed. The parameters of the roughness obtained from these measurements were rms height $\sigma = (4 \pm 0.5)$ Å, lateral correlation length $\xi = 3000$ Å, and vertical correlation length $\xi_z \geq 4000$ Å, which corresponded to a practically conformal roughness over all the interfaces. The effect of this roughness was expected to be revealed by high-resolution GID measurements.

The samples were adjusted for (220) GID in such a way that the x-ray beam formed a small angle with the sample surface close to the critical angle of total external reflection, $\Phi_c = 0.31^\circ$. At the same time the incident beam formed a Bragg angle with the atomic planes (110), which were perpendicular to the sample surface within the accuracy of miscut. The sample surface area illuminated by the x-ray beam at that incidence angle was about 10 mm in length.

The angular distribution of GID intensity reflected from the sample was analyzed either with a PSD [corresponding to the case shown in Fig. 1(c)] or with the Ge(220) analyzer crystal and PSD [corresponding to the scheme in Fig. 1(e)]. In the first case, the intensity distribution in the PSD (i.e. as a function of the takeoff angle Φ_h of the diffracted beam) was measured at a constant angle Φ_0 of incidence and different deviation angles $\delta\theta_2$ of the sample from the exact (220) diffraction position. Using the analyzer crystal, the distribution of GID intensity was additionally analyzed in the diffraction plane by the deviations $\delta\theta_3$ of the analyzer from the exact Bragg position.

IV. RESULTS AND DISCUSSION

A. Triple crystal measurements

Fig. 4 presents the set of PSD spectra measured from the Ge sample. The scheme of measurements corresponds to case (c) in Fig. 1. As in this case the PSD substitutes for an analyzer crystal; this scheme, by convention, can be referred to as a “triple” crystal one. The angle of incidence is Φ_0

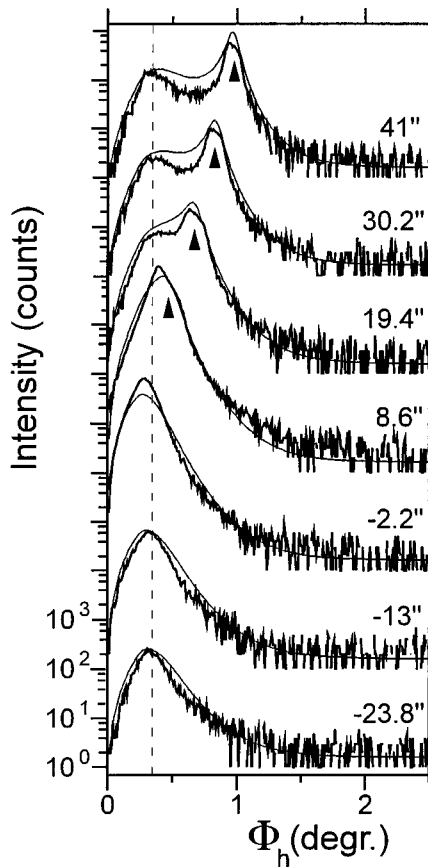


FIG. 4. Triple crystal curves [Fig. 1(c)] of GID obtained for a perfect Ge crystal. Experimental data and our calculations are shown by thick and thin lines respectively. The dashed line and the triangles show the positions of the sample and the collimator peaks respectively. The values of sample deviation from the exact GID position are given above the right wing of each curve.

$=0.3^\circ$ for all the curves, and the takeoff angle Φ_h is counted in the spectra from the direction along the sample surface with a step of 0.0078° corresponding to one channel of the PSD. The spectra in the figure are taken at different sample deviations from the exact GID position with a step of $\delta\theta_2 = 10.8''$.

As can be seen in Fig. 4, the spacing between the collimator and the sample peaks increases by increasing the sample deviation $\delta\theta_2$ in the diffraction plane. The positions of the collimator peak calculated according to Eq. (11) and indicated in Fig. 4 are in good agreement with experimentally measured ones. At negative $\delta\theta_2$, the collimator peak is absent in the curves, since the expression under the radical in Eq. (11) becomes negative because of the negative angle $\varphi_2 = -0.30^\circ$ of sample surface misorientation. The position of the sample peak remains fixed in all the curves in Fig. 4.

The theoretical spectra simulated according to Eq. (9) as a product of the GID curve from the sample and the Bragg curve from the collimator are shown in Fig. 4 by thin lines (the experimentally determined background has been added to all the theoretical curves). The approximation of the collimator diffraction curve by a Lorentzian function $1/(x^2+1)$ puts the theoretical and the experimental spectra

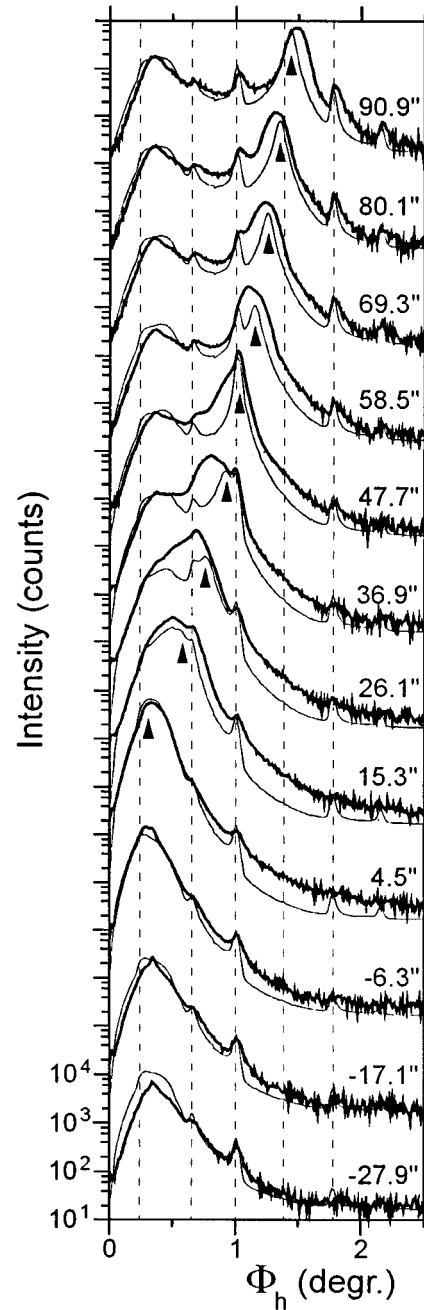


FIG. 5. Triple crystal curves [Fig. 1(c)] of GID obtained for an AlAs/GaAs superlattice. Experimental data and our calculations are shown by thick and thin lines respectively. The dashed lines and the triangles show the positions of the sample and the collimator peaks respectively. The values of sample deviation, $\delta\theta_2$, from the exact GID position are given above the right wing of each curve.

into better agreement than the use of a Darwin curve, although the latter produced sharper peaks.

The triple crystal curves for an AlAs/GaAs superlattice measured under the same experimental conditions as for the Ge sample are shown in Fig. 5. A number of superlattice peaks in fixed angular positions given by the Bragg law $\Phi_h = n\lambda/2(t_{\text{AlAs}} + t_{\text{GaAs}})$ are observed in the curves. The first maximum is shifted towards the right due to the refraction effect at the small takeoff angle. In contrast, the collimator peak flows with increasing angular deviation, $\delta\theta_2$, from the

exact diffraction condition. The positions of the collimator peak and the theoretical curves calculated in the same way as for the Ge sample display satisfactory agreement with the experimental data.

The collimator peaks on the angular spectra (Fig. 5) taken from the AlAs/GaAs superlattice do not exhibit any splitting. According to Eq. (14), it means that the superlattice is not relaxed. This fact was confirmed by conventional Bragg diffraction measurements from this sample.

Very valuable information that could be derived from a comparison of experimental to calculated data concerns the capability of separating coherent and diffuse scattering in GID. As explained above, the theoretical curves are calculated accounting for the coherent reflection from collimator and sample only. The satisfactory agreement of these curves with the experimental ones makes it evident that all the measured features around the collimator peak (the sample peak in Fig. 4 and the superlattice peaks in Fig. 5) correspond to the convolution of the sample diffraction curve with the wings of the collimator curve. Diffuse scattering is evidently weaker and is covered by coherent reflection. Consequently, the scheme, as it is, cannot be used to measure coherent and diffuse scattering separately.

B. Four crystal measurements

The GID measurements with the analyzer crystal and PSD were carried out at HASYLAB using the same experimental setup and the same superlattice as described above (Fig. 3). In this case the scheme of measurements can be referred to as a “four” crystal one. The measured curves are shown in Figs. 6 and 7. The two sets of curves in these figures correspond to two different offsets of the sample from the exact Bragg position: $\delta\theta_2 = 12''$ and $\delta\theta_2 = 30''$ for Fig. 6 and Fig. 7, respectively. The former offset corresponds to the maximum of the sample reflection coefficient. The PSD spectra in each figure are taken at different deviations $\delta\theta_3$ of the analyzer crystal from the Bragg position. The other parameters are the same as for the measurements without the analyzer.

Some peculiarities of four crystal curves can be pointed out. As the collimator is a single reflection crystal, its diffraction curve wings slope down as $1/x^2$ and therefore the superlattice peaks from the sample can be observed in the curves. The positions of these peaks are fixed.

There is a pronounced collimator peak in all the curves, and its position can be calculated according to Eq. (11). The results of the calculations are shown in Figs. 6 and 7. The position of the collimator peak is fixed for all curves at each figure, since the collimator-sample offset is constant.

Now, let us follow the analyzer peak positions. It can be seen from the modification of the most intense part of the central curves in Fig. 6 that at least one of two possible analyzer peaks shifts from left to the right. However, calculations with formula (12) and simulations of the theoretical curves with Eq. (10) did not agree well with the experimental data. Then, it was suggested that the analyzer crystal might be slightly misaligned from the vertical plane because of an inaccurate adjustment with respect to the double-plane collimated x-ray beam. By varying the angle of misalignment

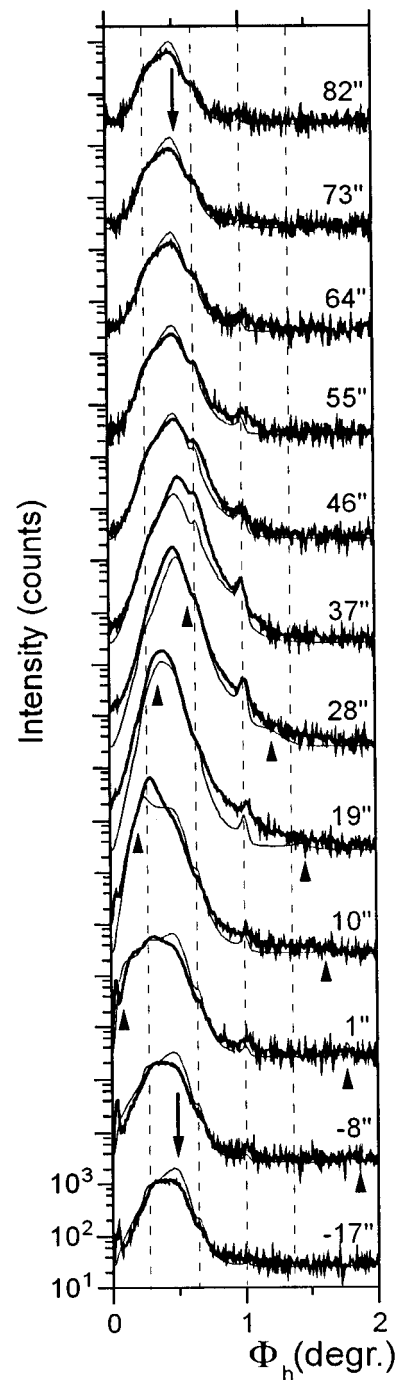


FIG. 6. Four crystal curves [Fig. 1(d)] of GID obtained for an AlAs/GaAs superlattice. The angle of sample deviation from the exact GID position is constant, $\delta\theta_2 = 12''$. Experimental data and our calculations are shown by thick and thin lines respectively. The dashed lines and the triangles show the positions of the sample and the analyzer peaks respectively. The fixed positions of the collimator peaks are marked by a thick arrow. The values of analyzer deviation, $\delta\theta_3$, from the exact Bragg position are given above the right wing of each curve.

φ_3 , the best fit for the positions of the analyzer peaks [calculated by formula (18)] and for the whole triple crystal curves was found at $\varphi_3 = -0.8^\circ$. It should be noted that when the angle of analyzer deviation becomes large enough, the expression under the radical in equation Eq. (18) be-

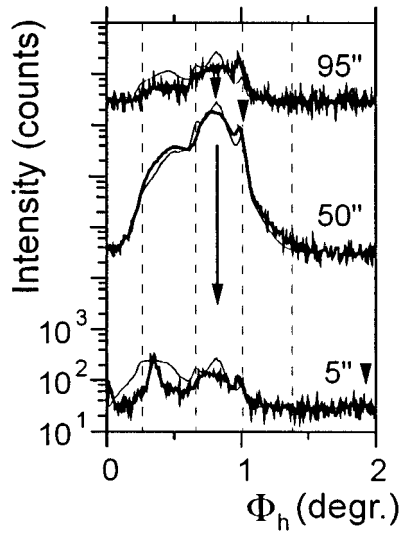


FIG. 7. Four crystal curves of GID obtained for an AlAs/GaAs superlattice. The angle of sample deviation from the exact GID position is constant, $\delta\theta_2 = 30''$. Experimental data and our calculations are shown by thick and thin lines respectively. The dashed lines and the triangles show the positions of the sample and the analyzer peaks respectively. The fixed positions of the collimator peaks are marked by a thick arrow. The values of analyzer deviation, $\delta\theta_3$, from the exact Bragg position are given above the right wing of each curve.

comes negative and the analyzer peaks are absent in the curves.

A good match of the calculations for the experiment, as was seen previously implies that diffuse scattering is not seen. Only at measurements on far wings of the sample curve, e.g., at $\delta\theta_2 = 30''$ in Fig. 7, may diffuse scattering play a role and this can be seen as a difference between theoretical and experimental curves. In general, accurate discrimination of coherent reflection from diffuse scattering requires collimator and analyzer diffraction curves without wings.

C. Triple crystal measurements with improved resolution

It is known that the wings of the diffraction curve can be suppressed by multiple diffraction, e.g., in a channel-cut crystal. The triple-crystal GID measurements Fig. 1(c) with application of a five-reflection channel-cut collimator and PSD were implemented on the optics beamline BL10 of the European Synchrotron Radiation Facility (ESRF). The details of the experiment are described elsewhere.⁴⁴

For a five-reflection collimator Eq. (9) transforms to

$$P_2^{\text{PSD}}(\Phi_h) \approx P^5(\alpha_1) P_{\text{GID}}[\alpha_1 + \alpha(\delta\theta_2)], \quad (19)$$

where the factor $P^5(\alpha_1)$ exhibits the Bragg peak at $\alpha_1 \approx 0$ with the angular halfwidth $\Delta\theta_{\text{col}}$ of a few angular seconds, while the wings of the peak drastically decrease $\sim 1/(\theta/\Delta\theta_{\text{col}})^{10}$ with the in-plane deviations θ of the x-rays. Thus, in this case the sample is practically illuminated at $\delta\theta_2 \pm \Delta\theta_{\text{col}}/2$, and according to Eq. (4) the takeoff angles of the diffracted x-rays are restricted by the narrow range $\Phi_h(\delta\theta_2) \pm \Delta\theta_{\text{col}} \sin(2\theta_B)/2\Phi_h(\delta\theta_2)$. The diffracted intensity at the other takeoff angles, if it exists, should be diffuse

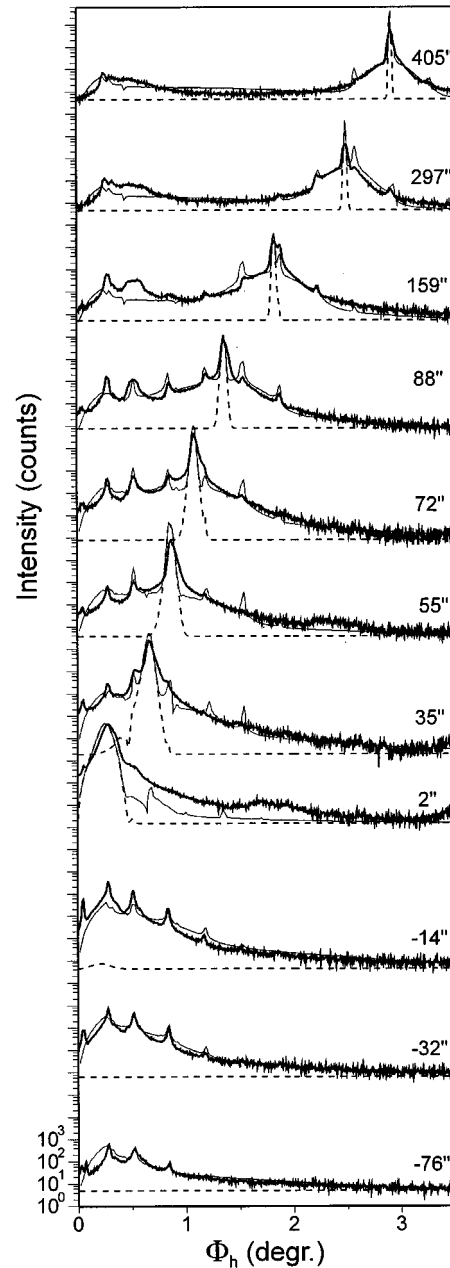


FIG. 8. Triple crystal curves of GID measured for an AlAs/GaAs superlattice at ESRF using a five-reflection channel-cut collimator. Experimental data are shown by thick solid lines. Calculated curves of coherent reflection and that with taking diffuse scattering from the interface roughness into account are plotted by dashed and thin solid lines, respectively. The values of sample deviation from the exact GID position, $\delta\theta_2$, are given above the right wing of each curve.

scattering. Thus, the increase in the in-plane resolution of the GID scheme improves resolution in the perpendicular direction (over the takeoff angles).

The experimental data for a AlAs/GaAs superlattice (the same sample that was discussed above), taken at $\lambda = 1.4 \text{ \AA}$, $\Phi_0 = 0.3^\circ$ and different deviations of the sample from the exact diffraction position are presented in Fig. 8. Two kinds of theoretical curves are compared with the experimental data (the experimental background is added to all theoretical curves). The theoretical curves are shown by dashed lines

calculated according to Eq. (19) as a product of coherent reflection from the collimator, approximated by the function $1/(x^2+1)^5$ (owing to the five reflections; $x=2\theta/\Delta\theta_{\text{col}}$), and the coherent part of GID from the sample. These curves do not coincide with the experimental ones and the difference (the wings of experimental curves around the collimator peak) can be attributed to diffuse scattering.

The thin solid curves are calculated by taking the diffuse scattering (DS) from the interfacial roughness in the AlAs/GaAs superlattice into account:

$$P_2^{\text{PSD}}(\Phi_h) \approx P_{\text{GID}}(\delta\theta_2) \delta[\Phi_h - \Phi_h(\delta\theta_2)] + I_{\text{DS}}(\Phi_h, \delta\theta_2), \quad (20)$$

where the expression for the DS intensity is⁴⁴

$$I_{\text{DS}} = \frac{k_0^3 \sin(2\theta_B) \Delta\theta_{\text{col}}}{16\pi^2 \Phi_0 \Phi_h} \times \sum_{k,n=1}^N \sum_{i,j=1}^4 \sum_{l,m=1}^2 C_{kil} \mathcal{D}_{ki}^{\text{in}} D_{kl}^{\text{out}} (C_{njm} \mathcal{D}_{nj}^{\text{in}} D_{nm}^{\text{out}})^* \times \int_{-\infty}^{\infty} dx [e^{Q_{kil} Q_{njm}^* \mathcal{R}_{kn}(x)} - 1] e^{q_x x}. \quad (21)$$

The summations in Eq. (21) are over $N=41$ interfaces in the 20 period period multilayer, over four wavefields $\mathcal{D}_{ki}^{\text{in}} = D_{0ki}^{\text{in}} \Delta\chi_h^k + D_{hki}^{\text{in}} \Delta\chi_0^k$ formed in each layer at the GID of incident wave, and over two wavefields D_{kl}^{out} formed at the specular reflection of scattered wave, respectively. The parameters $\Delta\chi_0$, $\Delta\chi_h$ are the jumps in x-ray polarizabilities at the interfaces, $C_{kil} = \exp(iQ_{kil}z_k - \sigma_k^2 Q_{kil}^2/2)/Q_{kil}$, z_k are the coordinates of the interfaces, Q_{kil} are the q_z -momentum transfers for different wavefields in the layers, and q_x is the momentum transfer along the surface in the direction perpendicular to \mathbf{k}_{h2}^B (see Fig. 2), which is the same for all the layers. Finally, $\mathcal{R}_{kn}(x)$ is the correlation function of roughness. We use the correlation function in the form by Ming *et al.*:⁴⁵ $\mathcal{R}_{kn}(x) = \sigma_k \sigma_n \exp(-x^2/\xi^2) \exp(-|z_k - z_n|/\xi_z)$. The parameters σ , ξ , and ξ_z are those measured by x-ray reflectivity and were given earlier. Eq. (21) gives diffuse scattering for scheme (c) in Fig. 1 where the scattered waves are integrated by PSD over their in-plane angular spread. For more details the reader is referred to Ref. 44.

When considering the roughness, the calculated curves in Fig. 8 are in satisfactory agreement with the experimental data. Although the superlattice peaks are observed in both Figs. 5 and 8, the peaks in the latter are not due to coherent diffraction but to diffuse scattering from interface-interface correlated roughness in the periodic multilayer. Thus, in the GID experiment application of the channel-cut collimator *in the plane of diffraction* improves the resolution function not only in this plane, but *in the perpendicular plane* as well and enables one to identify diffuse scattering.

However, the diffuse scattering measured is integrated with respect to the angular spread in the plane of diffraction. A detailed 3D mapping of GID will obviously require the four crystal scheme of Fig. 1(e) with the channel-cut collimator and the analyzer crystals. Further experiments are in progress.

V. CONCLUSIONS

The peculiarities of high-resolution measurements in GID and their applicability to discrimination between coherent reflection and diffuse scattering were considered both theoretically and experimentally. It was shown that the most information on structure and defects in the surface layers of crystals could be obtained with a two-dimensional angular analysis of scattered intensity using an analyzer crystal in the plane of diffraction and a PSD in the perpendicular plane. Such measurements correspond to the 3D mapping of reciprocal space.

Requirements of multiple crystal schemes were determined with respect to high-resolution GID measurements. It was shown that the application of non-dispersive crystal setting and the use of the channel-cut collimator and analyzer crystals were apt to improve the resolution function of GID experiments not only in the plane of diffraction but also in the perpendicular plane (over the takeoff angles).

Equations for the resolution function of GID experiments were derived and the positions of the sample, collimator and analyzer peaks were calculated and confirmed by experiment. The important influence of vertical misalignment of the analyzer was found experimentally and taken into account in the calculations.

Diffuse scattering from interfacial roughness in the AlAs/GaAs superlattice was discriminated experimentally from coherent GID using a non-dispersive five-reflection collimator and a PSD.

ACKNOWLEDGMENTS

The authors are grateful to R. Hey (PDI, Berlin) for the preparation of the AlAs/GaAs superlattice, and to A. Yu. Souvorov and J. U. Pfeiffer for help in the measurements at ESRF.

- ¹W. C. Marra, P. Eisenberger, and A. Y. Cho, J. Appl. Phys. **50**, 6927 (1979).
- ²A. M. Afanas'ev and M. K. Melkonyan, Acta Crystallogr. Sec. A **39**, 207 (1983).
- ³P. L. Cowan, S. Brennan, T. Jach, M. J. Bedzyk, and G. Materlik, Phys. Rev. Lett. **57**, 2399 (1986).
- ⁴T. Jach, P. L. Cowan, Q. Shen, and M. J. Bedzyk, Phys. Rev. B **39**, 5739 (1989).
- ⁵P. A. Aleksandrov, A. M. Afanas'ev, A. L. Golovin, R. M. Imamov, D. V. Novikov, and S. A. Stepanov, J. Appl. Crystallogr. **18**, 27 (1985).
- ⁶A. L. Golovin and R. M. Imamov, Phys. Status Solidi A **80**, K63 (1983).
- ⁷A. L. Golovin, R. M. Imamov, and E. A. Kondrashkina, Phys. Status Solidi A **88**, 505 (1985).
- ⁸R. M. Imamov, E. A. Kondrashkina, P. A. Aleksandrov, V. P. Grabchak, and O. V. Uvarov, Poverkhn. Fiz. Khim. Mekh. **3**, 41 (1987).
- ⁹S. Grotehans, G. Wallner, E. Burkel, H. Metzger, J. Peisl, and H. Wagner, Phys. Rev. B **39**, 8540 (1989).
- ¹⁰S. Rugel, G. Wallner, H. Metzger, and J. Peisl, J. Appl. Crystallogr. **26**, 34 (1993).
- ¹¹A. A. Williams, J. M. C. Thornton, J. E. Macdonald, R. G. van Silfhout, J. F. van der Veen, M. S. Finney, A. D. Johnson, and C. Norris, Phys. Rev. B **43**, 5001 (1991).
- ¹²V. H. Etgens, M. Sauvage-Simkin, R. Pinchaux, J. Massies, N. Jedrecy, A. Waldhauer, S. Tatarenko, and P. H. Jouneau, Phys. Rev. B **47**, 10607 (1993).
- ¹³U. Pietsch, H. Metzger, S. Rugel, B. Jenichen, and I. K. Robinson, J. Appl. Phys. **74**, 2381 (1993).
- ¹⁴D. Rose, U. Pietsch, A. Förster, and T. H. Metzger, Nucl. Instrum. Methods Phys. Res. B **97**, 333 (1995).

- ¹⁵P. Eisenberger, N. G. Alexandropoulos, and P. M. Platzman, *Phys. Rev. Lett.* **28**, 1519 (1972).
- ¹⁶B. C. Larson and W. Schmatz, *Phys. Rev. B* **10**, 2307 (1974).
- ¹⁷M. A. Pick, K. Bickman, E. Pofahl, K. Zwohl, and H. Wenzl, *J. Appl. Crystallogr.* **10**, 450 (1977).
- ¹⁸A. Iida and K. Kohra, *J. Appl. Phys.* **17**, 963 (1978); *Phys. Status Solidi A* **51**, 533 (1979).
- ¹⁹A. M. Afanas'ev, M. V. Kovalchuk, E. F. Lobanovich, R. M. Imamov, P. A. Aleksandrov, and M. K. Melkonyan, *Kristallografiya* **26**, 28 (1981) [*Sov. Phys. Crystallogr.* **26**, 13 (1981)].
- ²⁰P. Zaumseil and U. Winter, *Phys. Status Solidi A* **70**, 497 (1982).
- ²¹R. Pynn, Y. Fuji, and G. Shirane, *Acta Crystallogr. Sec. A* **39**, 38 (1983).
- ²²T. W. Ryan, P. D. Hatton, S. Bates, M. Watt, S. Sotomayor-Torres, P. A. Claxton, and J. S. Roberts, *Semicond. Sci. Technol.* **2**, 241 (1987).
- ²³C. A. Lucas, P. D. Hatton, S. Bates, T. W. Ryan, S. Miles, and B. K. Tanner, *J. Appl. Phys.* **63**, 1936 (1988).
- ²⁴C. A. Lucas, E. L. Gartstein, and R. A. Cowley, *Acta Crystallogr. Sec. A* **45**, 416 (1989).
- ²⁵E. L. Gartstein and R. A. Cowley, *Acta Crystallogr. Sec. A* **46**, 576 (1990).
- ²⁶B. K. Tanner and D. K. Bowen, *J. Cryst. Growth* **126**, 1 (1993).
- ²⁷P. F. Fewster, *Semicond. Sci. Technol.* **8**, 1915 (1993).
- ²⁸A. L. Golovin, R. M. Imamov, and S. A. Stepanov, *Acta Crystallogr. Sec. A* **40**, 225 (1984).
- ²⁹N. Bernhard, E. Burkel, G. Gompper, H. Metzger, J. Peisl, H. Wagner, and G. Wallner, *Z. Phys. B* **69**, 303 (1987).
- ³⁰U. Pietsch, H. Rhan, A. L. Golovin, and Yu. Dmitriev, *Semicond. Sci. Technol.* **6**, 743 (1991).
- ³¹S. A. Stepanov, U. Pietsch, and G. T. Baumbach, *Z. Phys. B* **96**, 341 (1995).
- ³²P. F. Fewster, *Appl. Phys. A* **58**, 121 (1994).
- ³³P. F. Fewster and N. L. Andrew, *J. Phys. D* **28**, A97 (1995).
- ³⁴The complete picture is obtained when the scans in Fig. 1(e) are taken at different incidence angles of the x-rays on the sample. The variations of the incidence angle are redundant in terms of the reciprocal space and the kinematical theory, but in a real experiment they control the depth and the illuminated area inside the sample.
- ³⁵A. M. Afanas'ev, P. A. Aleksandrov, R. M. Imamov, A. A. Lomov, and A. A. Zav'yalova, *Acta Crystallogr. Sec. A* **41**, 227 (1985).
- ³⁶A. M. Afanas'ev, S. M. Afanas'ev, P. A. Aleksandrov, A. A. Zav'yalova, R. M. Imamov, and A. A. Lomov, *Fiz. Tverd. Tela (Leningrad)* **27**, 2272 (1985) [*Sov. Phys. Solid State* **27**, 1365 (1985)].
- ³⁷A. M. Afanas'ev, P. A. Aleksandrov, A. A. Zav'yalova, R. M. Imamov, and A. A. Lomov, *Kristallografiya* **31**, 1066 (1986) [*Sov. Phys. Crystallogr.* **31**, 630 (1986)].
- ³⁸D. Bahr, W. Press, R. Jevasinski, and S. Mantl, *Phys. Rev. B* **51**, 12 223 (1995).
- ³⁹S. A. Stepanov, *Kristallografiya* **39**, 221 (1994) [*Crystallogr. Rep.* **39**, 182 (1994)].
- ⁴⁰S. A. Stepanov and R. Köher, *J. Phys. D* **27**, 1923 (1994).
- ⁴¹P. A. Alexandrov, A. M. Afanas'ev, and S. A. Stepanov, *Kristallografiya* **29**, 197 (1984) [*Sov. Phys. Crystallogr.* **29**, 119 (1984)].
- ⁴²S. A. Stepanov and R. Köhler, *J. Appl. Phys.* **76**, 7809 (1994).
- ⁴³A. P. Ulyanenko, S. A. Stepanov, U. Pietsch, and R. Köhler, *J. Phys. D* **28**, 2522 (1995).
- ⁴⁴S. A. Stepanov, E. A. Kondrashkina, M. Schmidbauer, R. Köhler, J.-U. Pfeiffer, T. Jach, and A. Yu. Souvorov, *Phys. Rev. B* **54**, 8150 (1996).
- ⁴⁵Z. H. Ming, A. Krol, Y. L. Soo, Y. H. Kao, J. S. Park, and K. L. Wang, *Phys. Rev. B* **47**, 16373 (1993).